Magnetic-free nonreciprocal photonic platform based on time-modulated graphene capacitors

D. Correas-Serrano, A. Alù, and J. S. Gomez-Diaz

Magnetic-free non-reciprocal photonic platform based on time-modulated graphene capacitors

D. Correas-Serrano[1], A. Alù[2,3,4], and J. S. Gomez-Diaz[1]*

[1]Department of Electrical and Computer Engineering, University of California Davis
One Shields Avenue, Kemper Hall 2039, Davis, CA 95616, USA.
[2]Photonics Initiative, Advanced Science Research Center, City University of New York
85 St. Nicholas Terrace, New York City, NY 10031, USA
[3]Physics Program, Graduate Center, City University of New York, New York 10016, USA
[4]Department of Electrical Engineering, City College of The City University of New York, New York 10031, USA
*E-mail: jsgomez@ucdavis.edu

We propose a novel paradigm for the realization of non-reciprocal photonic devices based on time-modulated graphene capacitors coupled to photonic waveguides, without relying on magneto-optic effects. The resulting hybrid graphene-dielectric platform is low-loss, silicon-compatible, robust against graphene imperfections, scalable from terahertz to near infrared frequencies, and it exhibits large nonreciprocal responses using realistic biasing schemes. We introduce an analytical framework based on solving the eigenstates of the modulated structure and on spatial coupled mode theory, unveiling the physical mechanisms that enable nonreciprocity and enabling a quick analysis and design of optimal isolator geometries based on synthetic linear and angular momentum bias. Our results, validated through harmonic balance full-wave simulations, confirm the feasibility of the introduced low-loss (<3 dB) platform to realize large photonic isolation through various mechanisms, such as narrowband asymmetric bandgaps and interband photonic transitions that allow multiple isolation frequencies and large bandwidths. We envision that this technology may pave the wave to magnetic-free, fully-integrated, and CMOS-compatible nonreciprocal components with wide applications in photonic networks and thermal management.

1. Introduction

Lorentz reciprocity ensures that the response of a linear device is unchanged when excitation and observation points are swapped [1], [2]. This is a fundamental property that has limited the way in which electromagnetic signals are processed and transmitted. Non-reciprocal systems, which are not bounded by this symmetry, have become of critical importance throughout the entire frequency spectrum to realize devices like circulators and isolators, enabling radar operation, full-duplex communications, and to protect sensitive laser sources from reflections.

Non-reciprocity has traditionally been achieved through magneto-optical effects, requiring lossy and bulky magnetic materials under strong biasing fields that are incompatible with modern technology trends, in constant pursuit of miniaturized, integrated, and affordable devices. Motivated by these shortcomings, recent years have seen a rapidly growing interest on alternative ways to break reciprocity, mainly through nonlinear materials [3]–[5] and spatiotemporal modulation, able to impart linear or angular momentum to the wave propagation within the system [2], [6]–[9]. Although nonlinear isolators do not require an external bias, they are limited in their operation to a range of high intensity signals and excitation from a single port at a time [4]. The modulation approach is intensity-independent and it provides greater design flexibility, which has allowed researchers to put forward a wide variety of magnet-less non-reciprocal devices in electromagnetics and acoustics [2], [10]–[12]. Unfortunately, the use of this concept in practical applications beyond radio-frequencies remains challenging due to the high modulation frequencies required –not achievable with common switches or varactors– and the difficulty of rapidly modulating the properties of optical materials [11], [13]. Recently, gated graphene structures with time-varying biasing voltages have been introduced as a promising platform to implement this paradigm at THz and IR, owing to the ultrafast modulation that it can support and the numerous attractive features of graphene plasmonics [6], [14]–[18]. However, this approach requires high-quality graphene able to support plasmons with low damping. This is critical not only for acceptable levels of insertion loss, but also for sufficiently strong non-reciprocal responses, as the spectral linewidth of the resonant states affects how effectively they exchange energy when not perfectly phase-matched. Such interaction is especially significant when the modulation frequency is much smaller than the operation frequency, leading to spurious coupling that becomes an additional source of loss [2], [6].

To reduce the burden on graphene quality, here we propose to break reciprocity by using spatiotemporally modulated graphene as a *perturbation* of high-Q photonic modes in dielectric structures. The resulting hybrid graphene-dielectric photonic devices are low-loss, silicon-compatible, frequency-scalable from THz to infrared and telecom wavelengths, robust against graphene imperfections, and exhibit large non-reciprocal responses using realistic biasing schemes. We emphasize the compatibility of this platform with well-known integrated photonic systems, as graphene is used here *only* to engineer the required non-reciprocal coupling between photonic states, having negligible effect on their impedance, wavenumber and field profile. Moreover, the unprecedented performance at IR frequencies makes this platform suitable to break emission and absorption symmetries in thermal management applications, such as thermophotovoltaic cells with increased efficiency [19]. We illustrate the capabilities and broad reach of this platform by designing and analyzing different types of isolators based on linear and angular momentum. Several configurations are explored, including isolators based on asymmetric bandgaps able to achieve arbitrarily large isolation over a narrow bandwidth, and on interband photonic transitions that enable larger operation

bandwidth. To fully understand the operation principle of this platform, illustrate their underlying physical mechanisms, and to quickly analyze and design optimal components, we introduce an analytical framework based on solving the eigenstates of the modulated structure and on spatial coupled mode theory, and use harmonic balance full-wave simulation to verify our predictions. Our platform can significantly outperform other magnetic-free nonreciprocal solutions in photonics at terahertz, IR, and telecom wavelengths, which typically rely on lossy PIN junctions [13], [20]–[22] or on narrowband optomechanical effects [23]–[28].

2. Isolators based on asymmetric bandgaps

Consider the structure of Fig. 1a, where a pair of closely spaced graphene sheets have been transferred on the two sides of a dielectric slab with permittivity ε_2 surrounded by media ε_1 and ε_3. For deeply subwavelength separation, the graphene stack has an effective conductivity that is simply the sum of the two layers, i.e., $\sigma_{stack} \approx \sigma_1 + \sigma_2$, and it can be modulated by applying a voltage between them, enabling broad control of the stack conductivity [29]. This configuration, employing a single capacitor, has been used to experimentally realize optical modulators with speeds as high as 30 GHz [30], with suboptimal contact resistance being the limiting factor. Speeds close to 100 GHz would be possible with state-of-the-art low-resistance contacts, which would further boost the performance of the platform proposed here [31], [32]. If multiple of these capacitors are placed along the propagation direction z of a waveguide, shown in Fig. 1b, one can synthesize through well-known relations the voltages required to yield a spatially and temporarily varying conductivity profile of the form [6], [12], [16], [29], [30]

$$\sigma_{eff}(z,t) = \sigma_{stack}(1 + M \cdot cos(\omega_m t - k_m z)), \tag{1}$$

where M is the modulation depth, t is time, ω_m is the modulation frequency, and $k_m = 2\pi/p$ is the modulation wavenumber, p being the spatial period. This effective conductivity will be exploited below to implement various types of photonic isolators. Note that, because of the smooth voltage between adjacent capacitors, edge effects are expected to have a small influence [33], and the required modulation depth is smaller than in the experimentally-demonstrated modulators mentioned above, as those devices require large voltage swings to switch critical coupling on and off [30]. These two considerations provide an optimistic outlook for potential experimental demonstrations of the devices proposed below.

We begin by considering an isolator based on asymmetric bandgaps for the fundamental transverse electric (TE) mode of the dielectric waveguide in Fig. 1. It is well known that a periodic perturbation to a waveguide can be used to engineer photonic bandgaps, in which the propagation constant acquires an imaginary part associated to back-scattering [34]. This is the operation principle behind Bragg gratings [35], [36]. The isolator proposed here is based on a similar principle, but the time-varying nature of the perturbation now frequency-shifts the bandgaps in opposite directions for left-right and right-left propagation. This is analogous to the Doppler effect that would be observed if a Bragg grating was physically moving along the z-axis [2], [37]. For instance, Ref. [37] analyzed the properties of asymmetric photonic bandgaps for plane waves propagation in an infinite dielectric medium where the permittivity is modulated along the propagation direction, and experimentally demonstrated this concept around 2.5 GHz by means of varactors modulated at 675 MHz. Unfortunately, that approach would be unfeasible at THz or IR frequencies because varactors cannot be modulated fast enough [2], [38], [39]. This limitation of varactors applies to any non-reciprocal device based on spatiotemporal modulation, not just to the isolators presented in this section. Because of this, researchers in photonics have focused on modulating the properties of optical materials like silicon using PIN junctions, an approach that is limited by weak achievable modulation indexes, high loss, and fabrication complexity [11]–[13]. The platform presented in the following is intended to overcome these challenges.

Propagation through the isolator of Fig. 1b can be quantitatively analyzed by computing the eigenstates of the spatiotemporally modulated system, which provide the complex-valued propagation constant within the bandgap for both propagation directions. We start by writing the TE fields as an infinite summation of momentum-frequency harmonics [40],

$$E_{y1} = \sum_{i=-\infty}^{\infty} A_i e^{j\omega_i t} e^{-jk_{x1i} x} e^{-jk_{zi} z}$$

$$E_{y2} = \sum_{i=-\infty}^{\infty} (B_i \cos(k_{x2i} x) + C_i \sin(k_{x2i} x)) e^{j\omega_i t} e^{-jk_{zi} z} \tag{2}$$

$$E_{y3} = \sum_{i=-\infty}^{\infty} D_i e^{j\omega_i t} e^{+jk_{x3i} x} e^{-jk_{zi} z},$$

where $k_{xni} = \sqrt{\varepsilon_{rn} k_{0i}^2 - k_{zi}^2}$ is the x-component of the wavenumber in the medium n for the ith harmonic, A, B, C and D are amplitude constants, and the graphene stack is located at $x = 0$. The associated magnetic field is given by Maxwell's equations. Enforcing continuity of the tangential fields across the interfaces through the usual current boundary condition on graphene $\hat{n} \times (\boldsymbol{H}_1 - \boldsymbol{H}_2) = \sigma_{eff}(z,t)\boldsymbol{E}_t$, we find the general dispersion relation of the modulated structure for an arbitrary number of harmonics:

Figure 1. Hybrid dielectric-graphene isolator based on asymmetric bandgaps. (a) Dielectric waveguide loaded with a time-modulated graphene capacitor. (b) Photonic isolator based on a dielectric waveguide (y-invariance is assumed) with relative permittivities $\varepsilon_1 = \varepsilon_3 = 4$ (SiO$_2$) and $\varepsilon_2 = 12$ (Si), $h = 2.75\ \mu m$, loaded with a series of time-modulated graphene capacitors with interlayer spacing much smaller than h, resulting in an effective conductivity along z of the form shown in Eq. (1), with $M = 0.3$, $\omega_m = 30$ GHz and $k_m = 8.52 \cdot 10^6$. Overlaid is the associated y-component of the guided mode (not to scale). Panels (c), (d) show the real and imaginary parts of the wavenumber of the guided mode near the bandgap, computed analytically for both propagation directions. (e) Isolation and insertion loss versus graphene relaxation time for a waveguide length of 1.5 mm. (f) Poynting vector for excitation from the left (energy is transmitted to the right) and from the right (energy is frequency converted and reflected). Graphene chemical potential and relaxation time are 0.4 eV and 1 ps, modulation frequency is 30 GHz, modulation index is 0.3, and temperature is 300 K.

$$\sum_{i=-\infty}^{\infty} e^{j\omega_i t} \frac{A_i}{\omega_i \mu_0} \left(j k_{xi2} c_b - k_{xi1} \right) = \sigma_{eff} \sum_{i=-\infty}^{\infty} e^{j\omega_i t} A_i e^{-j\beta_i z} e^{-jk_{x1}x}, \tag{3}$$

where

$$c_b = \frac{\left(-\frac{jk_{xi2}}{k_{xi3}} \sin(k_{x2i}h) - \cos(k_{x2i}h) \right)}{\left(-\sin(k_{x2i}h) + \frac{jk_{xi2}}{k_{x3}} \cos(k_{x2i}h) \right)}. \tag{4}$$

In the absence of modulation, the harmonics are decoupled and the above dispersion relation describes standard TE modes, taking the form

$$\frac{1}{\omega_i \mu_0} \left(j c_b k_{xi2} - k_{xi1} \right) = -\sigma_{stack}. \tag{5}$$

Unsurprisingly, this expression is similar to the textbook solution of the fundamental surface wave in a dielectric slab [34], and it will be used in the following to apply coupled mode theory to the analysis and design of this and other types of isolators. The modulation given by Eq. (1) introduces coupling among harmonics, which, given the perturbing nature of the modulation, we can safely assume to be limited to the neighboring harmonics, resulting in the following infinite set of equations

$$e^{j\omega_i t} \frac{A_i}{\omega_i \mu_0} \left(j c_b k_{xi2} - k_{xi1} \right) = \sigma_{stack} \left(A_i + \frac{A_{i+1}M}{2} + \frac{A_{i-1}M}{2} \right) e^{j\omega_i t} \tag{6}$$

which can be truncated to a few terms to yield a determinant equation that can be solved for k_{xi1} and thus k_{zi}, fully characterizing all Fourier harmonics through their wavenumber $k_{zi} \pm n k_m$ and frequency $\omega \pm n\omega_m$. Note that we have

neglected the influence of the conductivity dispersion since $\omega_m \ll \omega_0$. It can easily be taken into account in the Drude regime by writing the conductivity as $\sigma_g(z,t) = \sigma_0(z,t)/(1+j\omega\tau)$, which allows to separate the modulated Drude weight from its frequency dispersion. We have verified that the influence of this correction is negligible, as long as $\omega_m \ll \omega_0$.

Figs. 1c-d show the real and imaginary parts of the fundamental harmonic wavenumber near the bandgap for such a waveguide, with the values for left-right and right-left propagation plotted along the same axis for easy visualization. The key feature enabling isolation is apparent in Fig. 1d, which shows the frequency-shifted attenuation factors $\text{Im}[k_z]$ due to the bandgap. If the excitation frequency lies within a range where only positive or negative k_z have a large imaginary part, arbitrarily large isolation can be achieved by increasing the waveguide length, since power will be gradually reflected in that direction, but not in the opposite one. Importantly, the frequency of reflected waves is $f_0 \pm f_m$. Fig. 1e shows the isolation and insertion loss of a 1.5 mm-long isolator based on this principle versus graphene phenomenological relaxation time [16], showing a good isolation to loss ratio for moderate to high quality graphene. Relaxation times greater than 0.5 ps have been experimentally realized in recent years, so these results are encouraging for practical implementations [41], [42]. Fig. 1f, computed with harmonic-balance full-wave simulations in COMSOL Multiphysics [43], demonstrates the operation of the device, showing full transmission for excitation from the left (left column), and reflection and conversion to a different harmonic for excitation from the right (right column), in close agreement with our theory. In particular, the figure shows the z-component of the Poynting vector when the isolator is excited from both directions at $f_0 = 10.01\,\text{THz}$. Note that the figure has a largely distorted scale in the two dimensions for the sake of visualization, as the waveguide height is $2.75\,\mu m$ and the isolator length is $1.5\,mm$.

An ideal approach to study these problems is based on the coupled mode formalism [34], [36]. This framework is well suited not only to validate the response presented earlier, but also to design and analyze different types of isolators like the one shown in the next section, owing to its generality, and to provide physical insights in their operation. Coupled mode theory (CMT) describes the space or time evolution of overlapping modes in coupled resonators or waveguides, and it has been extensively used to model couples, filters, and more recently non-reciprocal acoustic and electromagnetic devices based on spatiotemporal modulation [10], [12], [44], [45]. For two waves with amplitudes a_1 and a_2 and propagation constants k_{z1} and k_{z2}, weakly coupled by some means, their coupled mode equations in space may be written as [12], [34]

$$\frac{da_1}{dz} = -jk_{z1}a_1 + \kappa_{12}a_2$$
$$\frac{da_2}{dz} = -jk_{z2}a_2 + \kappa_{21}a_1 \tag{7}$$

If the modes do not interact, $\kappa_{ij} = 0$ (with $i \neq j$) and the decoupled equations simply describe the amplitude variation given by the propagation constants k_{zi}. For coupled modes, the coupling coefficients κ_{ij} determine the rate with which the modes exchange power and, if power is to be conserved, $\kappa_{12} = \kappa_{21}^* = \kappa$ [36]. This operation is typically mediated by a perturbation to the permittivity such as $\varepsilon = \varepsilon(x,y) + \delta\varepsilon(x,y)\cos(\omega_m t - k_m z)$, resulting in the well-known, general expression for the coupling coefficient [12], [34], [45]

$$\kappa = -\frac{j\omega}{4} \iint \delta\varepsilon(x,y)\boldsymbol{E_1}(x,y)\boldsymbol{E_2^*}(x,y)dxdy \tag{8}$$

The platform proposed here relies instead on modulating graphene's conductivity, and its practical feasibility compared to other solutions depends largely on the capability of this modulation to perturb high-Q dielectric modes. Once this has been quantified, any non-reciprocal electromagnetic device based on linear or angular momentum bias can be designed. We show in the appendix that the coupling coefficient in this case is

$$\kappa = \frac{M}{8}\sigma_{stack}\boldsymbol{E}_1^{(t)}\boldsymbol{E}_2^{(t)*}, \tag{9}$$

where $\boldsymbol{E}_i^{(t)}$ is the tangential field of the ith mode on graphene's surface, normalized to a power flow of 1 Watt along $\hat{z}$, i.e. $\iint \boldsymbol{E}_i \times \boldsymbol{H}_i^* dxdy = 2$ [34]. Therefore, the coupling coefficient between any two modes interacting with graphene is simply the scalar product of the tangential electric fields on graphene, weighted by the perturbation to the conductivity. If multiple graphene stacks were present throughout the structure, all the contributions should be added. The applicability of Eq. (9) extends far beyond the context of this paper, as it allows analytical treatment of any nonreciprocal device based on time-modulated graphene, including isolators, circulators, metasurfaces, or antennas [6], [8], [12], [19], [45]–[47], by simply solving for the relevant eigenmodes. Plasmonic devices, where graphene acts as the main propagation platform via surface plasmon polaritons rather than as a perturbation, will also benefit from this approach. These devices inherently suffer from higher loss and they require graphene of very high quality, but they may be a suitable choice when extreme miniaturization or tunability are required. Refs. [6], [14] put forward isolators, non-reciprocal antennas and phase-shifters based on this mechanism, and we envision that the framework derived here will lead to a refinement of these concepts and near-optimal designs. We note that this discussion also applies to temporal coupled mode theory, typically used to study resonant structures [8], [36].

In this context, the operation mechanism of the isolator of Fig. 1, based on asymmetric bandgaps, can also be understood as non-reciprocal coupling of two modes at f_0 and $f_0 \pm f_m$ propagating in opposite directions. This perspective allows to take
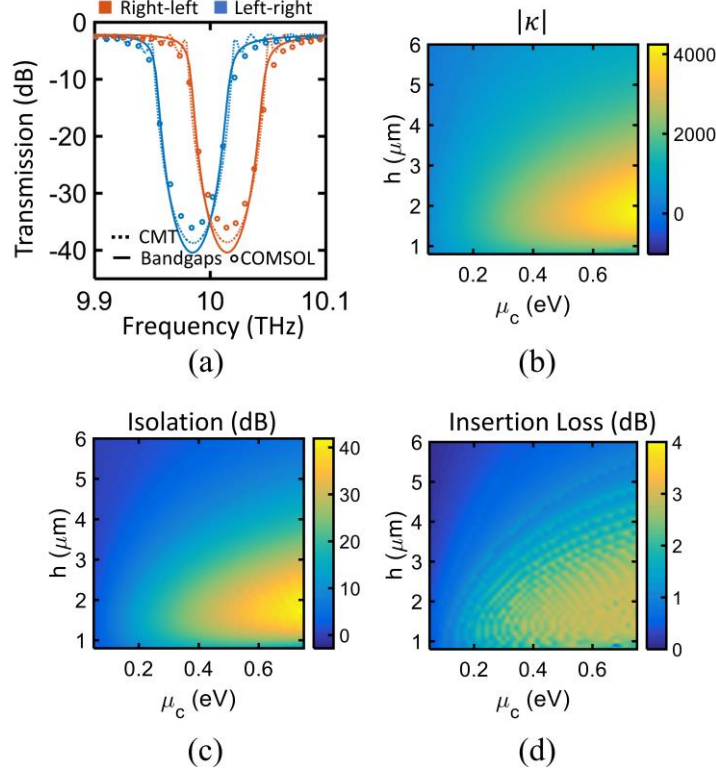
Figure 2. (a) Bidirectional transmission of the isolator from Figure 1, computed with three different approaches: (i) considering the propagation decay in the bandgaps given by Eq. (3), (ii) applying coupled mode theory with the dispersion and field profiles of the unmodulated waveguide given by Eq. (5); and (iii) using harmonic balance full-wave simulation in COMSOL Multiphysics. (b)-(d) Parametric study of coupling coefficient, isolation, and insertion loss of the proposed isolator versus waveguide height and chemical potential of the graphene sheets. Parameters are the same as in Fig. 1.

advantage of the system respose in the absence of any modulation, given by Eqs. (2) and (5), in conjunction with Eq. (7) [34], [36]. For any two modes to efficiently exchange power, phase matching conditions must hold so that the fields scattered along the structure's length add constructively, meaning $\omega_m = \omega_2 - \omega_1$, $\Delta k = k_{z2}(\omega_0 \pm \omega_m) - k_{z1}(\omega_0) - k_m = 0$ (in the present case, k_{z1} and k_{z2} have opposite signs). It should not be surprising that this is precisely the design condition for the frequencies and wavenumbers at which the asymmetric bandgaps appear.

Fig. 2a validates the accuracy of both theoretical approaches, showing the transmission for both propagation directions predicted by the dispersion approach (using Eq. (6)), CMT and harmonic-balance full-wave simulations in COMSOL Multiphysics. In the latter, we excite the structure at ω_0 and introduce modulation-induced coupling to adjacent harmonics through surface currents on graphene, with magnitudes obtained by expanding the boundary condition $J_{stack}(z,t) = \sigma_{eff}(z,t)E_i^{(t)}(z,t)$ and identifying terms at ω_0 and $\omega_0 \pm \omega_m$. Figs. 2b-d explore the design space using CMT to compute the coupling coefficient κ, isolation, and insertion loss for a wide range of waveguide heights and graphene chemical potentials, allowing to visualize performance trade-offs. In this particular case, there is an optimal range of heights that maximize isolation, whereas a monotonic dependence is observed versus chemical potential.

Lastly, we demonstrate in Fig. 3 the possibility of reducing the footprint of this type of isolators by using a resonant, spatiotemporally moduled ring coupled to an unmodulated bus waveguide, achieving a 10-fold reduction in device length. This is similar to the device proposed in [46], modulating the ring permittivity and using an additional bus waveguide. All mode coupling now takes place within the ring, forming a resonant state that is a hybridization of the forward mode at ω_0 and the frequency-converted reflected mode at $\omega_0 \pm \omega_m$, due to the bandgap [2], [12], [45], [46]. The modulation parameters are the same as in the linear-waveguide case, but now the bus-ring separation must also be designed for critical coupling [48]. In this example, this separation is 5.1 μm, and ring radius is 34.5 μm.

Engineered photonic bandgaps have far reaching implications beyond the devices shown in this section, where we have only explored the proof-of-concept case of an ideal sinusoidal modulation and monomode excitation. This simple scenario provides remarkable isolation performance and valuable insight into the underlying physics, but one could also envision other exotic responses based on more complex space-time modulation schemes, or by using the spatiotemporally modulated structure as a non-reciprocal scatterer. For instance, Ref. [49] studied varactor-based modulations that are periodic in time but aperiodic in
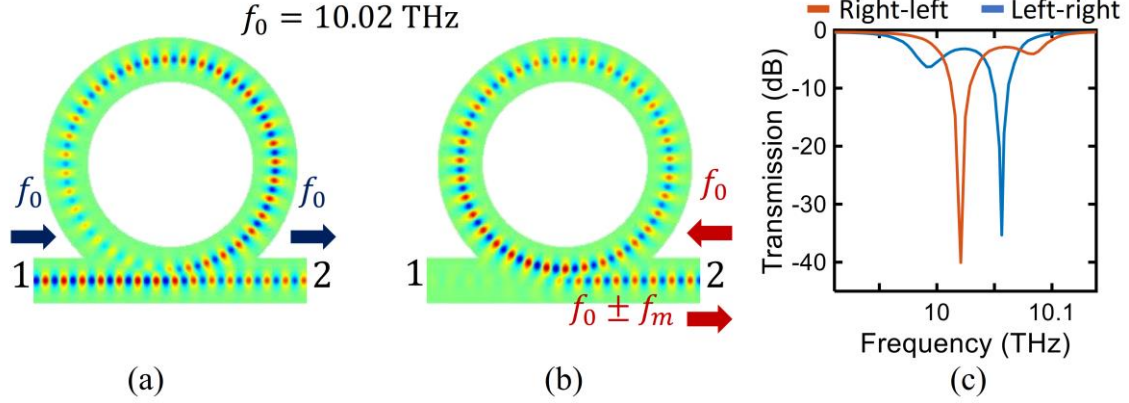
Figure 3. Compact implementation of the hybrid dielectric/graphene isolator in Figs 1-2. By using a graphene-modulated resonant ring coupled to a standard, unmodulated bus waveguide, mode coupling occurs within the resonant ring and a 10-fold length reduction is achieved. Parameters are as in Figs 1-2, ring radius is 39 μm, and distance between bus and waveguide is 5 μm.

space, which yields large aperiodic bandgaps that can be used for pure frequency mixing and isolation while forbidding undesired transitions thanks to carefully designed strong dispersion; and Ref. [50] studied transmission of plane waves through a spatiotemporally a modulated slab, showing angle-dependent non-reciprocal harmonic generation and filtering. These concepts could in principle be translated to the hybrid graphene-photonic platform proposed here, enabling their application at THz and IR frequencies. Another topic worth exploring relates to the so-called quasi-sonic operation, when the phase velocity of carrier signal, $v_0 = \omega_0/k_z$, is similar to the phase velocity of the modulated signal, $v_m = \omega_m/k_m$ [51], [52]. This leads to interesting phenomena such as all harmonics merging into a single dispersion curve, as discussed in [50] for scattering by a infinite quasisonic slab. However, for devices operating at THz and IR, $\omega_m \ll \omega_0$ necessarily, and thus $v_m \ll v_0$ unless $k_m \ll k_0$, so they typically operate in a deeply subsonic regime, as is the case in the devices studied here. Nonetheless, it may be possible to design hybrid graphene-dielectric structures where $v_0 \approx v_m$ through deliberate dispersion engineering.

3. Isolators based on interband photonic transitions

In this section we explore a different approach to realize magnet-free isolators, using a similar modulation scheme to couple otherwise orthogonal modes in a multimode structure, so that in the isolated direction all power is converted to a different mode that can be filtered or scattered. In the connected direction, phase matching does not hold and thus no conversion occurs. This class of isolator has been considered in [12], [13], [53] for dielectric waveguides with spatiotemporally modulated permittivity, and in [6] for all-graphene plasmonic devices. The operation principle, illustrated in Fig. 4a, is quite general and provides important advantages over the bandgap-based approach of the previous section in terms of enhanced operation bandwidth and simplified modulation scheme, as k_m is typically smaller –in this type of diagram, the isolator of the previous section would be based on coupling between the forward and backward red or blue curves, a much bigger jump in the momentum axis. This type of mode conversion is usually termed 'interband photonic transition' in analogy with electron transitions between bands in semiconductors [2]. Importantly, full power exchange between modes propagating in the same direction occurs periodically, with a period equal to the so-called coherence length, which is inversely proportional to the coupling coefficient $L_c = \pi/2|\kappa|$ [2]. The modulated region should therefore extend an odd multiple of coherence lengths –there is no benefit in making it greater than one, but this condition means that isolation could also occur at higher frequencies.

Fig. 4b depicts a structure capable of realizing this response. The device is identical to the one in Fig. 1, except for the additional requirement that the waveguide must support at least two modes, achieved here by increasing the waveguide height. The dispersion of the even and odd modes is computed using Eq. (5), which allows to suitably select the modulation parameters. Fig. 4c shows a snapshot of the fields at f_0 and $f_0 + f_m$ for the isolated direction, demonstrating how the input mode (with even symmetry, fundamental TE mode) is completely converted to the odd-symmetric mode over the coherence length. We show an enlarged view of the ports for the sake of visualization, as the device is significantly longer (1.8 mm). In practice, this isolator would likely be connected to single-mode waveguides through a tapered section that would at the same time serve as a filter for the higher order mode carrying power in the isolated direction. Fig. 4d shows the dispersion of the modes, and Fig. 4e depicts the transmission for both directions versus frequency, computed using CMT (solid lines) and full-wave simulations in COMSOL Multiphysics (circle markers), once again demonstrating isolation greater than 20 dB and low loss. This result also highlights an important advantage of this type of isolators: *bandwidth engineering*. Because the dispersion of the modes involved can be engineered a priori through the geometrical parameters and choice of materials, it is indeed possible to achieve the phase-matching condition over a wider frequency range if the dispersion curves are close to parallel, as roughly achieved in this isolator between 8.8 and 10 THz. This comes at the cost of increased device footprint compared to the resonant implementation of Fig. 3, a trade-off often found in non-reciprocal devices based on spatiotemporal modulation [2]. In addition, the same structure can simultaneously support isolation for different directions at different frequencies, as also evidenced by
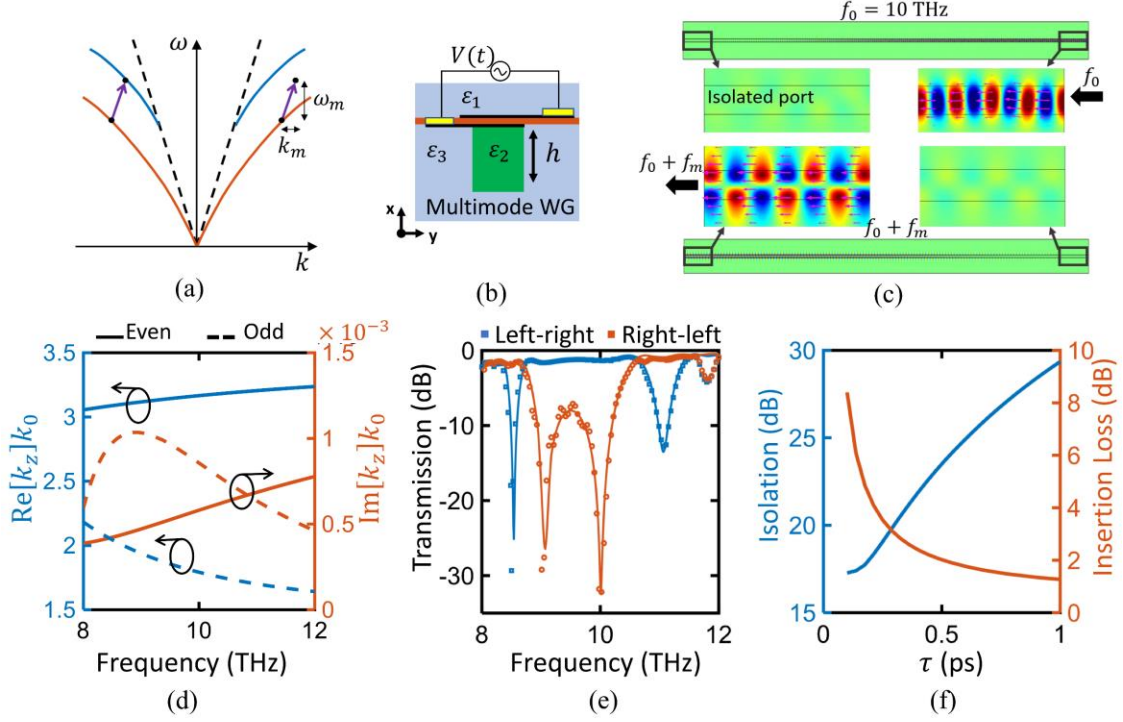
Figure 4. Hybrid graphene/dielectric isolator based on interband photonic transitions. (a) Operation principle: if $\omega_m = \omega_2 - \omega_1$ and $k_{mod} = k_2 - k_1$, perfect phase matching occurs and total power conversion occurs between the orthogonal modes. This happens only in one direction. Dashed black and solid red and blue lines denote the light cone and even and odd modes, respectively. (b) Transverse view of a multimode waveguide able to host this type of isolator. (c) Full-wave simulation of an isolator based on this principle, for the isolated direction. Shown are enlarged snapshots of the ports for better visualization. Device length is 1.36 mm waveguide height h is 6 μm (d) Dispersion of the even and odd modes involved in the operation. (e) Transmission for both propagation directions, computed with coupled mode theory (solid lines) and full-wave simulations (markers). (f) Isolation and insertion loss versus graphene relaxation time. Graphene's chemical potential and relaxation time are 0.4 eV and 1 ps, respectively, modulation frequency is 30 GHz, $k_m = 1.86 \cdot 10^5$, modulation index is 0.3, and temperature is 300 K.

this design around 8.2 and 11 THz. Finally, Fig. 4f shows the isolation and insertion loss at 10 THz versus graphene's relaxation time, confirming that the reported response is moderately robust versus graphene's quality. Another important difference between this type of isolators and those based on asymmetric bandgaps concerns the modulation profile in the transverse plane: because the modes are orthogonal, the perturbation applied to the waveguide must be asymmetric in x for κ to not vanish [12]. Consider, for instance, an additional modulated set of graphene capacitors at the bottom of the waveguide, resulting in an additional contribution to Eq. (9). If both modulations were in phase, the two contributions would be of equal magnitude and opposite, leading to $\kappa = 0$. Note that this is not the case in the bandgap-based implementation, where the coupling coefficient would instead double.

The proposed platform is quite general and can be implemented up to infrared frequencies using various waveguide configurations, such as a pair of coupled monomode waveguides supporting even and odd supermodes. The advantage of this structure lies in the similarity of the supermode dispersion curves, which results in smaller values of the modulation wavenumber k_m and therefore fewer bias connections and simpler practical realization. This concept was realized in [13] at 1.55 μm by modulating the permittivity of silicon waveguides through PIN junctions, but their highly lossy nature considerably limited overall performance –yielding a measured isolation of 3 dB with an insertion loss of 70 dB. In Fig. 5a we propose a similar structure operating at telecom wavelengths where modulation is instead provided by graphene capacitors. The design has been once again carried out with CMT and validated with COMSOL Multiphysics, without any optimization. Theoretically predicted isolation is greater than 60 dB, as modes have almost identical (low) damping, whereas numerical results predict roughly 35 dB due to numerical noise. Insertion loss is less than 3 dB and it remains almost constant versus graphene's relaxation time τ, since it is mainly caused by spurious coupling between the modes rather than absorption. The odd mode carrying power in the isolated direction would in practice be removed at the ports, for instance by using multimode interference waveguides (MMI), as done experimentally in [13]. Lastly, we note that graphene should be sufficiently doped to prevent excessive absorption by electron interband transitions, i.e. $2\mu_c > \hbar\omega$, a condition that is met here. The excellent performance and reduced modulation complexity of this type of isolator make it particularly suited for near-infrared integrated silicon-photonics devices.
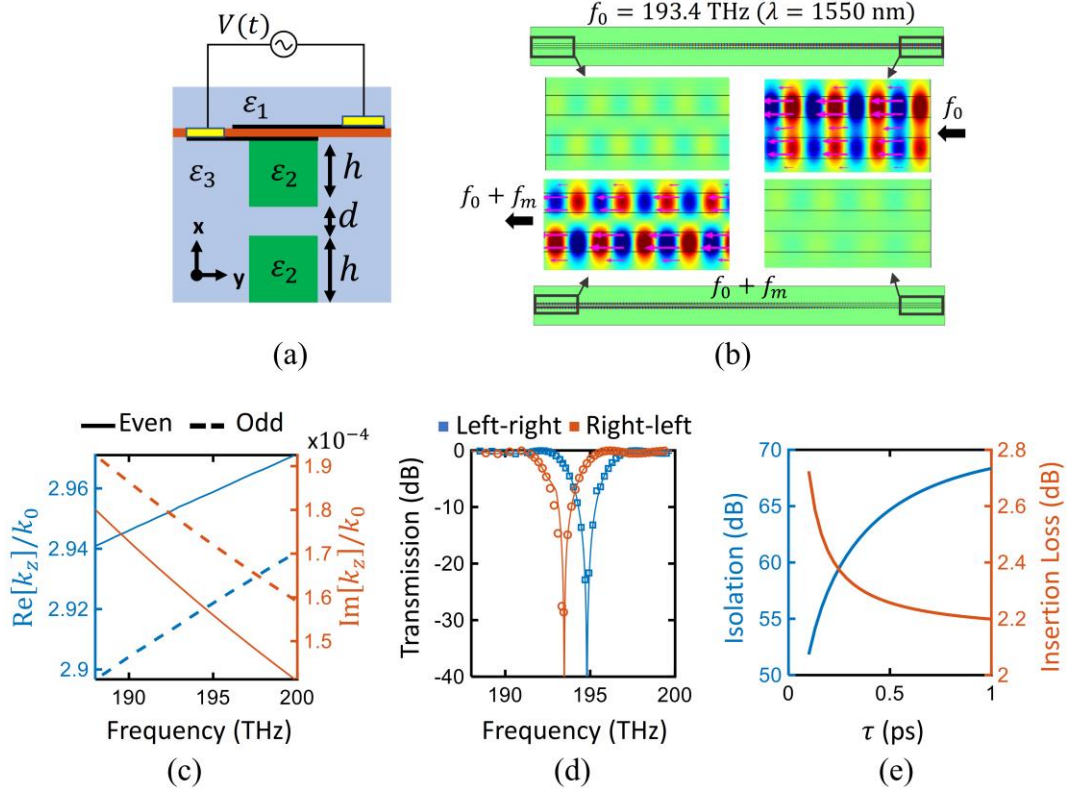
Figure 5. Hybrid graphene/dielectric isolator based on interband photonic transitions operating at $\lambda = 1550$ nm. Operation is like in Fig. 4, but instead of using a single multimode wire, two coupled monomode wires supporting even and odd supermodes are used [11]. The advantage of this approach lies in it requiring smaller k_{mod}, since the modes have similar wavenumbers, making it suitable for short wavelengths. (a) Transverse view of the waveguide. (b) Full-wave simulation in the isolated direction at $\lambda = 1550$ nm. An enlarged view of the ports is shown for better visualization. (c) Dispersion of the quasi- even and odd supermodes (d) Transmission for both propagation directions, computed with coupled mode theory (solid lines) and full-wave simulations (markers). (e) Isolation and insertion loss versus graphene relaxation time. Device length is 1.26 mm, waveguide height h is 300 nm, separation d is 300 nm, graphene's chemical potential and relaxation time are 0.7 eV and 1 ps, modulation frequency is 30 GHz, $k_m = 1.53 \cdot 10^5$, modulation index is 0.3, and temperature is 300 K.

We have established here the foundation for manipulating interband photonic transitions in hybrid graphene-dielectric devices through simple, effective devices; but the core physics is quite general, and we expect that a much wider range of THz and IR devices will be demonstrated in the future by borrowing concepts from the rapidly growing literature on spatiotemporally modulated media. For instance, a system of two waveguides coupled in a Mach-Zehnder interferometer configuration, with one of them spatiotemporally modulated, can realize circulation and isolation [53], [54]; or the photonic transition can take place in resonant rings to reduce device footprint [12], as we did in the previous section for bandgap-based isolators. This type of photonic transition can also enable circulation of scattered free-space waves, as shown in [8] for a dielectric slab with modulated permittivity. We have focused in this paper on linear momentum biasing, but our proposed platform is also perfectly suitable for angular momentum biased devices such as the modulated ring of Fig. 3. Angular momentum may allow to reduce the complexity of modulation schemes even further, for instance by using three coupled resonators that are time-modulated with phase differences of 120 degrees [2], [11], [55]. This phase difference provides the spatial part of the modulation in a way that circumvents the potential practical difficulties of discretizing a continuous modulation profile [2]. The simplest translation of this concepts into our platform would consist of three coupled dielectric resonators perturbed by time-modulated graphene capacitors. More sophisticated schemes at RF have been proposed in [11], [56], [57], and they could in principle be similarly adapted. It is also possible to break reciprocity by considering coupled resonators with different resonant frequencies and modulating the coupling between them [2], [58]. This vast landscape of possibilities, combined with the ongoing efforts on streamlining graphene fabrication and modulation processes, paints a promising picture for practical, integrated, non-reciprocal photonic devices for THz and IR in the near future.

4. Conclusions

Hybrid dielectric-graphene waveguides form an ideal platform to realize low-loss, magnetic-free, silicon-compatible, nonreciprocal components from terahertz up to near-infrared frequencies. This platform combines the robustness and promise of silicon photonics with the simplicity of modulating graphene conductivity to engineer non-reciprocal coupling of modes, which we quantified in a general analytical form. We also introduced a framework based on solving the eigenstates of the

structure and on spatial coupled mode theory to describe the physical mechanisms that enable nonreciprocity and to efficiently design and analyze realistic devices. Specifically, narrowband isolators implemented through asymmetric bandgaps and isolators with large bandwidth relying on interband photonic transitions have been put forward and investigated. Results, validated with full-wave numerical simulations, confirm the outstanding performance of the proposed technology and its robustness versus graphene's loss. Even though we have limited our analysis in this paper to isolators, the versatility and far-reaching implications of this platform should be emphasized: it can in principle be employed to develop low-loss photonic circulators, Faraday rotators, as well as to manipulate nonreciprocity at the micro/nano scale to realize advanced functionalities such as nonreciprocal beam-steering and lensing, among others. More importantly, this technology overcomes multiple challenges of the state of the art in terms of CMOS-compatibility and integration, miniaturization, losses, and performance. We envision that this paradigm will lead to a new generation of nonreciprocal photonic components with wide implications in sensing, communication systems, optical networks, and thermal management.

Appendix. Coupling of modes analysis of graphene-dielectric isolators

Here we provide a detailed derivation for the coupling coefficient for two modes interacting via a modulated conductive surface such as the ultra-thin graphene stack considered in the paper, starting from familiar formalisms within the coupling of modes framework [2], [34], [36]. Expressions for transmission through the waveguide for both types of isolators are also provided. Typically, coupling of modes along a direction z is mediated by a periodic modulation of the permittivity $\varepsilon = \varepsilon_{static} + \delta\varepsilon(z,t)$, where the perturbation $\delta\varepsilon$ can be written as a Fourier series expansion

$$\delta\varepsilon = \sum_{n \neq 0} \varepsilon_n \, e^{-jn(k_m z - \omega_m t)} \tag{10}$$

In order to reconcile the conductivity modulation considered here with this approach, we take advantage of an equivalent way to describe a sheet with conductivity σ_g, by considering it as a thin slab of thicknes $t_g \ll \lambda$ and permittivity ε_g [59]. Assuming an $\exp(j\omega t)$ time variations, this permittivity is

$$\varepsilon_g = \varepsilon_0 - j\frac{\sigma_g}{\omega t_g}. \tag{11}$$

The equivalent permittivity of the graphene stack under the modulation of Eq. (1) can thus be expressed as

$$\varepsilon_{stack} \approx -j\frac{\sigma_{stack}}{\omega t_g}\left(1 + \frac{M}{2}e^{-j(k_m z - \omega_m t)} + \frac{M}{2}e^{+j(k_m z - \omega_m t)}\right) \tag{12}$$

where we safely neglected the term associated to the free-space permittivity as it is orders of magnitude smaller than $j\frac{\sigma_g}{\omega t_g}$. For the expansion of Eq. (10), we have

$$\varepsilon_{\pm 1} = \frac{M}{2}\frac{j\sigma_{stack}}{\omega t_g} \tag{13}$$

The coupling integral in Eq. (8) could now be solved using this permittivity and the corresponding fields inside and outside the equivalent graphene slab. However, it is far more convenient from both a theoretical and numerical point of view to retain the surface conductivity description and the associated fields, such as those given by Eq. (2). Combining Eqs. (8), (11), (13), recalling that $t_g \ll \lambda$, and integrating over the waveguide cross-section, we can write

$$\kappa_{21} = \frac{M}{8}\iint \sigma_{eff}(y)E_1^{(t)}E_2^{(t)*}dxdy \tag{14}$$

where $E_i^{(t)}$ is the electric field tangential to graphene. Assuming invariance in y and σ_{eff} located in the x-y plane, it reduces to Eq. (9), which can also be written as $\kappa = \frac{M}{8}A_1 A_2 \sigma_{stack}$. Compared to Eq. (8), the fields E_i must be replaced by their tangential components $E_i^{(t)}$, because an infinitesimally thin conductive sheet cannot support currents along the perpendicular axis. This is not an approximation: if the electromagnetic problem were instead solved within the equivalent thin-slab formalism, computing the fields "inside" graphene, one would find (for both TE and TM waves) strictly zero polarization current along the normal, and a non-zero uniform current in the tangential directions, providing fully consistent results [60].

For the isolator based on asymmetric bandgaps, assuming low absorption, solving Eq. (7) allows to find the power transmission through the device as [34]

$$T = e^{2\text{Im}\left[k_z^{(\omega_0)}\right]L} \left(1 - \frac{|\kappa|^2 \sinh^2 sL}{s^2 \cosh^2 sL + (\Delta k_z/2)^2 \sinh^2 sL}\right) \tag{15}$$

where

$$s^2 = |\kappa|^2 - \left(\frac{\Delta k}{2}\right)^2 \tag{16}$$

with $\Delta k = k_{z2}(\omega_0 \pm \omega_m) - k_{z1}(\omega_0) - k_m$, as defined in the main text. The peak value of the reflectivity for a waveguide of length L is

$$R = \frac{|\kappa|^2 L^2}{1 + |\kappa|^2 L^2} \tag{17}$$

For the isolators based on interband photonic transitions, the field amplitude evolution of the two modes along the waveguide reads [12]

$$A_1(z) = e^{\text{Im}\left[k_z^{(\omega_0)}\right]z} e^{-j\Delta k/2} \left[\cos(zs) + j \frac{\Delta k/2}{s} \sin(zs)\right] \tag{18}$$
$$A_2(z) = e^{\text{Im}\left[k_z^{(\omega_0 \pm \omega_m)}\right]z} e^{j\Delta k/2} \frac{C \sin(zs)}{s}$$

Within this modeling framework, non-reciprocity in both cases arises due to the different values of Δk entering Eqs. (16) and (17) for opposite propagation directions.

Acknowledgement

References

[1]   H. B. G. Casimir, On Onsager's principle of microscopic reversibility, Rev. Mod. Phys. 17, 343–350 (1945).
[2]   D. L. Sounas and A. Alù, Non-reciprocal photonics based on time modulation, Nat. Photonics 11, 774–783 (2017).
[3]   D. L. Sounas and A. Alù, Time-Reversal Symmetry Bounds on the Electromagnetic Response of Asymmetric Structures, Phys. Rev. Lett. 118, 154302 (2017).
[4]   Y. Shi, Z. Yu, and S. Fan, Limitations of nonlinear optical isolators due to dynamic reciprocity, Nat. Photonics 9, 388–392 (2015).
[5]   D. L. Sounas, J. Soric, and A. Alù, Broadband passive isolators based on coupled nonlinear resonances, Nat. Electron. 1, 113–119 (2018).
[6]   D. Correas-Serrano, J. S. Gomez-Diaz, D. L. Sounas, Y. Hadad, A. Alvarez-Melcon, and A. Alù, Nonreciprocal Graphene Devices and Antennas Based on Spatiotemporal Modulation, IEEE Antennas Wirel. Propag. Lett. 15, 1529–1533 (2016).
[7]   T. Kodera and C. Caloz, Integrated leaky-wave antenna-duplexer/diplexer using CRLH uniform ferrite-loaded open waveguide, IEEE Trans. Antennas Propag. 58, 2508–2514 (2010).
[8]   Y. Shi, S. Han, and S. Fan, Optical Circulation and Isolation Based on Indirect Photonic Transitions of Guided Resonance Modes, ACS Photonics 4, 1639–1645 (2017).
[9]   S. Taravati, Self-biased broadband magnet-free linear isolator based on one-way space-time coherency, Phys. Rev. B 96, 235150 (2017).
[10]   R. Fleury, D. L. Sounas, C. F. Sieck, M. R. Haberman, and A. Alù, Sound isolation and giant linear nonreciprocity in a compact acoustic circulator, Science 343, 516 (2014).
[11]   N. A. Estep, D. L. Sounas, and A. Alù, Magnetless microwave circulators based on spatiotemporally modulated rings of coupled resonators, IEEE Trans. Microw. Theory Tech. 64, 502–518 (2016).
[12]   Z. Yu and S. Fan, Complete optical isolation created by indirect interband photonic transitions, Nat. Photonics 3, 91–94 (2009).
[13]   H. Lira, Z. Yu, S. Fan, and M. Lipson, Electrically driven nonreciprocity induced by interband photonic transition on a silicon chip, Phys. Rev. Lett. 109, 033901 (2012).
[14]   C. Qin, B. Wang, H. Long, K. Wang, and P. Lu, Non-reciprocal Phase Shift and Mode Modulation in Dynamic Graphene Waveguides, J. Light. Technol. 8724, 3877-3883 (2016).

[15] K. Geim and K. S. Novoselov, The rise of graphene, Nat. Mater. 6, 11-19 (2007).

[16] A. H. Castro Neto, F. Guinea, N. M. R. Peres, K. S. Novoselov, and A. K. Geim, The electronic properties of graphene, Rev. Mod. Phys. 81, 109–162 (2009).

[17] R. Z. Zhang and Z. M. Zhang, Tunable positive and negative refraction of infrared radiation in graphene-dielectric multilayers, Appl. Phys. Lett. 107, 11–16 (2015).

[18] D. A. Smirnova, A. V. Gorbach, I. V. Iorsh, I. V. Shadrivov, and Y. S. Kivshar, Nonlinear switching with a graphene coupler, Phys. Rev. B 88, 045443 (2013).

[19] Y. Hadad, J. C. Soric, and A. Alù, Breaking temporal symmetries for emission and absorption, Proc. Natl. Acad. Sci. 113, 3471–3475 (2016).

[20] V. R. Almeida, C. A. Barrios, R. R. Panepucci, and M. Lipson, All-optical control of light on a silicon chip, Nature 431, 1081–1084 (2004).

[21] Q. Xu, B. Schmidt, S. Pradhan, and M. Lipson, Micrometre-scale silicon electro-optic modulator, Nature 435, 325–327 (2005).

[22] Q. Xu, B. Schmidt, J. Shakya, and M. Lipson, Cascaded silicon micro-ring modulators for WDM optical interconnection, Opt. Express 14, 9431 (2006).

[23] F. Ruesink, M. A. Miri, A. Alù, and E. Verhagen, Nonreciprocity and magnetic-free isolation based on optomechanical interactions, Nat. Commun. 7, 13662 (2016).

[24] M. A. Miri, F. Ruesink, E. Verhagen, and A. Alù, Optical Nonreciprocity Based on Optomechanical Coupling, Phys. Rev. Appl. 7, 064014 (2017).

[25] N. R. Bernier, L. D. Toth, A. Koottandavida, M. A. Ioannou, D. Malz, A. Nunnenkamp, A. K. Feofanov, and T. J. Kippenberg, Nonreciprocal reconfigurable microwave optomechanical circuit, Nat. Commun. 8, 604 (2017).

[26] M. A. Miri, E. Verhagen, and A. Alù, Optomechanically induced spontaneous symmetry breaking, Phys. Rev. A 95, 053822 (2017).

[27] F. Ruesink, J. P. Mathew, M. A. Miri, A. Alù, and E. Verhagen, Optical circulation in a multimode optomechanical resonator, Nat. Commun. 9, 1798 (2017).

[28] K. Fang, J. Luo, A. Metelmann, M. H. Matheny, F. Marquardt, A. A. Clerk, and O. Painter, Generalized non-reciprocity in an optomechanical circuit via synthetic magnetism and reservoir engineering, Nat. Phys. 13, 465–471 (2017).

[29] J. S. Gomez-Diaz, C. Moldovan, S. Capdevila, J. Romeu, L. S. Bernard, A. Magrez, A. M. Ionescu, and J. Perruisseau-Carrier, Self-biased reconfigurable graphene stacks for terahertz plasmonics, Nat. Commun. 6, 6334 (2015).

[30] C. T. Phare, Y. D. Lee, J. Cardenas, and M. Lipson, Graphene electro-optic modulator with 30 GHz bandwidth, Nat. Photonics 9, 511–514 (2015).

[31] W. S. Leong, H. Gong, and J. T. L. Thong, Low-contact-resistance graphene devices with nickel-etched-graphene contacts, ACS Nano 8, 994–1001 (2014).

[32] W. Li, Y. Liang, D. Yu, L. Peng, K. P. Pernstich, T. Shen, A. R. Hight Walker, G. Cheng, C. A. Hacker, C. A. Richter, and Q. Li, Ultraviolet/ozone treatment to reduce metal-graphene contact resistance, Appl. Phys. Lett. 102, 183110 (2013).

[33] D. Correas-Serrano, J. S. Gomez-Diaz, J. Perruisseau-Carrier, and A. Alvarez-Melcon, Graphene-based plasmonic tunable low-pass filters in the terahertz band, IEEE Trans. Nanotechnol. 13, 1145 (2014).

[34] A. Yariv and P. Yeh, Optical waves in crystals, Wiley, New York (1984).

[35] R. Kashyap, Fiber Bragg gratings, Academic Press (2010).

[36] H. Haus, Waves and Fields in Optoelectronics, Prentice-Hall (1985).

[37] N. Chamanara, S. Taravati, Z. L. Deck-Léger, and C. Caloz, Optical isolation based on space-time engineered asymmetric photonic band gaps, Phys. Rev. B 96, 155409 (2017).

[38] C. Caloz, A. Alù, S. Tretyakov, D. Sounas, K. Achouri, and Z.-L. Deck-Leger, What is Nonreciprocity? Part I, IEEE Antennas Wirel. Propag. Lett. 17 (2018).

[39] C. Caloz, A. Alù, S. Tretyakov, D. Sounas, K. Achouri, and Z.-L. Deck-Léger, What is Nonreciprocity? Part II, IEEE Antennas Wirel. Propag. Lett. 17 (2018).

[40] E. S. Cassedy and A. A. Oliner, Dispersion Relations in Time-Space Periodic Media: Part I—Stable Interactions, Proc. IEEE 51, 1342–1359 (1963).

[41] A. Woessner, M. B. Lundeberg, Y. Gao, A. Principi, P. Alonso Gonzalez, M. Carrega, K. Watanabe, T. Taniguchi, G. Vignale, M. Polini, and J. Hone, Highly confined low-loss plasmons in graphene–boron nitride heterostructures, Nat. Mater. 14, 421–425 (2014).

[42] P. Alonso-González, A. Y. Nikitin, Y. Gao, A. Woessner, M. B. Lundeberg, A. Principi, N. Forcellini, W. Yan, S. Velez, A. J. Huber, K. Watanabe, T. Taniguchi, L. E. Hueso, M. Polini, J. Hone, F. H. L. Koppens, and R. Hillenbrand, Acoustic terahertz graphene plasmons revealed by photocurrent nanoscopy, Nat. Nanotech. 12, 31 (2016).

[43] COMSOL Multiphysics, https://www.comsol.com/.

[44] A. Yariv, Coupled-mode theory for guided-wave optics, IEEE J. Quantum Electron. 9, 919–933 (1973).

[45] D. L. Sounas, C. Caloz, and A. Alù, Giant non-reciprocity at the subwavelength scale using angular momentum-biased metamaterials, Nat. Commun. 4, 2407 (2013).

[46] D. L. Sounas, and A. Alù, Angular-Momentum-Biased Nanorings To Realize Magnetic-Free Integrated Optical Isolation, ACS Photonics 1, 198–204 (2014).

[47] S. Taravati and C. Caloz, Mixer-Duplexer-Antenna Leaky-Wave System Based on Periodic Space-Time Modulation, IEEE Trans. Antennas Propag. 65, 442–452 (2017).

[48] A. Yariv, Critical coupling and its control in optical waveguide-ring resonator systems, IEEE Photonics Technol. Lett. 14, 2001–2003 (2002).

[49] S. Taravati, Aperiodic space-time modulation for pure frequency mixing, Phys. Rev. B 97, 115131 (2018).

[50] S. Taravati, N. Chamanara, and C. Caloz, Nonreciprocal Electromagnetic Scattering from a Periodically Space-Time Modulated Slab and Application to a Quasi-Sonic Isolator, Phys. Rev. B 96, 165144 (2017).

[51] S. T. Peng, E. S. Cassedy, and B. R. Rao, The sonic region for propagation in a parametric medium with harmonic pump modulation, Proc. IEEE 57, 224–225 (1969).

[52] R.-S. Chu and T. Tamir, Guided-wave theory of light diffraction by acoustic microwaves, IEEE Trans. Microw. Theory Tech. 18, 486–504 (1970).

[53] Z. Yu, and S. Fan, Integrated Nonmagnetic Optical Isolators Based on Photonic Transitions, J. Sel. Top. Quantum Electron. 16, 459–466 (2010).

[54] S. Bhandare, S. K. Ibrahim, D. Sandel, H. Zhang, F. Wüst, and R. Noé, Novel nonmagnetic 30-dB traveling-wave single-sideband optical isolator integrated in III/V material, IEEE J. Sel. Top. Quantum Electron. 11, 417–421 (2005).

[55] N. A. Estep, D. L. Sounas, J. Soric, and A. Alù, Magnetic-free non-reciprocity and isolation based on parametrically modulated coupled-resonator loops, Nat. Phys. 10, 923 (2014).

[56] A. Kord, D. L. Sounas, and A. Alù, Magnetless Circulators Based on Spatiotemporal Modulation of Bandstop Filters in a Delta Topology, IEEE Trans. Microw. Theory Tech. 66, 911 (2018).

[57] A. Kord, D. L. Sounas, and A. Alù, Pseudo-Linear Time-Invariant Magnetless Circulators Based on Differential Spatiotemporal Modulation of Resonant Junctions, IEEE Trans. Microw. Theory Tech. 66 (2018).

[58] N. Bergeal, F. Schackert, M. Metcalfe, R. Vijay, V. E. Manucharyan, L. Frunzio, D. E. Prober, R. J. Schoelkopf, S. M Girvin, and M. H. Devoret, Phase-preserving amplification near the quantum limit with a Josephson ring modulator, Nature 465, 64 (2010).

[59] A. Vakil and N. Engheta, Transformation Optics Using Graphene, Science 332, 1291 (2011).

[60] D. Correas-Serrano, A. Alù, and J. S. Gomez-Diaz, Plasmon canalization and tunneling over anisotropic metasurfaces, Phys. Rev. B 96, 075436 (2017).